Modeling Time-varying Sea Surface Effects on Seismic Data using Mimetic Finite Differences

Tugrul Konuk and Jeffrey Shragge
Center for Wave Phenomena, Colorado School of Mines

ABSTRACT
Temporal and spatial variations in the sea surface during seismic acquisition are often ignored in seismic data processing flows that commonly assume a flat free surface. However, weather patterns during acquisition can generate rough sea conditions, which influence source and receiver ghost reflections and surface-related multiples by introducing spatially and temporally varying distortions of the seismic wavelet. To investigate the rough sea effects on seismic wave propagation, we develop a mimetic finite-difference time-domain (MFDTD) scheme based on fully staggered grids to solve the 3D acoustic wave equation. We employ a dynamic (i.e., moving) generalized coordinate system conformal to the time-varying free surface. The time-varying coordinate mapping leads to a static Cartesian computational mesh, but with time-varying coefficients on the mimetic gradient and divergence operators. This allows us to model the full dynamic effects associated with this complex free-surface boundary condition. Numerical examples demonstrate that the MFDTD method can accurately simulate seismic wave propagation on a moving mesh and is a reliable tool for modeling, processing, imaging, and inversion of seismic data acquired in rough seas.

Key words: mimetic, rough sea, finite-difference, acoustic, ghost, multiples

1 INTRODUCTION

Seismic data processing flows often ignore sea conditions during data acquisition and assume an idealized flat sea surface. However, rough sea conditions introduce spatially and temporally varying amplitude and phase perturbations to any seismic event that interacts with the sea surface, such as source and receiver ghost and surface-related multiples. Inaccurately handling these effects [e.g., inaccurate deghosting and surface-related multiple elimination (SRME)] can severely decrease data quality and penalize seismic data resolution. Laws and Kragh (2002) investigate the rough sea effects on time-lapse seismic data and report that RMS amplitude errors are between $5-10\%$ even with a relatively calm sea with 2 m of significant wave height (SWH). Therefore, ignoring or inaccurate handling of rough sea effects may influence a wide range of applications including 3D/4D full-wavefield seismic modeling, imaging, and inversion studies.

Modeling a realistic time-varying free-surface boundary is an essential step when investigating the wave scattering from dynamic rough sea surfaces. In this study, we use the Pierson and Moskowitz (1964) spectrum to generate time-varying sea surface models because of its straightforward numerical approach in describing realistic sea states. This model assumes a fully developed sea where a wind with a constant velocity vector has been blowing for a long period of time and sea surface has established a steady state.

There are numerous approaches to modeling the effects of rough sea surfaces on seismic data with varying degrees of physical accuracy. Ogilvy (1987), Thorsos (1988), and Egorov et al. (2018) use the Kirchhoff-based modeling approaches to the simulate seismic wavefield interacting with rough sea surfaces generated with the Pierson-Moskowitz spectrum. Kirchhoff-based methods are accurate only for near-normal-incidence scattering due to their smooth sea-surface assumption. In addition, they are unable to provide the multiply scattered part of the seismic wavefield and thus incorrectly model free-surface multiples important for SRME. Laws and Kragh (2002) also investigates the rough sea effects on seismic repeatability using the Kirchhoff method and a finite-difference based modeling algorithm that requires

significant grid refinement to accurately represent rough surfaces. However, none of these methods can model the full wave propagation effects (i.e., both kinematics and dynamics) while simultaneously incorporating a time-varying free-surface boundary.

Finite-difference methods are a natural choice to model the complete seismic wavefield response, but conventional Cartesian-based finite-difference operators fail to simultaneously represent the physical properties of the governing equations and the boundary conditions. Even though finite elements (FE) methods may provide a global high-order accuracy at both interior regions and the free-surface (Komatitsch and Vilotte, 1998), they require complicated meshing procedures, which would be subject to time-varying stability restrictions and would have to represent all the sharp discontinuities in the model while maintaining an optimal grid size.

In this work, we develop a mimetic finite-difference (MFD) scheme for solving the 2D acoustic wave equation [AWE, Shragge and Tapley (2017)] in a dynamic (i.e., moving) generalized coordinate mesh that naturally incorporates the time-varying free-surface boundary and the associated free-surface boundary condition. We define a straightforward finite-difference scheme by transforming the generalized 4D tensorial gradient and divergence operators and associated geometric fields from a time-varying deformed Cartesian mesh to a regularly sampled, time-independent generalized coordinate system using a unique one-to-one mapping relationship (Shragge and Tapley, 2017). The coordinate transformation introduces additional cross-derivative terms that are absent from the original AWE for isotropic media. We adopt 2D fully staggered grids [FSG, Lebedev (1964); Lisitsa and Vishnevsky (2010)] to calculate these additional derivatives. The 2D FSG comprises a set of two complementary staggered grids and provides all the required derivatives for the AWE-MFD solution of the AWE. To obtain accurate solutions near the mesh boundaries, we implement MFD operators (Castillo and Miranda, 2013; de la Puente et al., 2014) that provide a uniform numerical accuracy throughout the computational domain.

This paper focuses on the modeling and investigation of the rough sea effects on seismic data. We introduce a modeling scheme for seismic wavefield propagation on time-varying grids and a mimetic methodology for accurately implementing the free-surface boundary condition. To test the stability of the developed algorithm, we conduct a test with exaggerated sea height and wave speed. We further investigate more realistic scenarios and provide three numerical modeling examples to demonstrate the rough sea effects on seismic data. Our results show that time-varying rough seas introduce non-trivial and non-linear phase and amplitude perturbations to the seismic wavefield. These effects, if not considered during data processing, would severely reduce the reliability of any seismic data processing procedure requiring a sea surface profile (e.g., deghosting, demultiple, time-lapse seismic data processing).

2 THEORY

The tensorial acoustic wave equation in a 3D generalized coordinate system is given by (Shragge and Tapley, 2017)

$$\left[\nabla_\xi^2 - \frac{1}{c_\xi^2}\frac{\partial^2}{\partial t^2}\right] P_\xi = F_\xi, \tag{1}$$

where subscript $\boldsymbol{\xi}$ indicates a quantity in the generalized coordinate system, c_ξ is the speed of sound in the medium, P_ξ is the scalar pressure field, F_ξ is the source term, and ∇_ξ^2 is the tensorial Laplace-Beltrami operator. Here, the fields and operations are converted from an irregularly shaped time-varying physical domain in the Cartesian coordinate system $\mathbf{x}(t) = [t, x_1(t), x_2(t), x_3(t)]$ to a regularly sampled time-independent computational domain in a generalized coordinate system $\boldsymbol{\xi}(\tau) = [\tau, \xi_1(\tau), \xi_2(\tau), \xi_3(\tau)]$, where $\tau = t$ (see Figure 1). Given that a unique mapping relationship between the $\boldsymbol{\xi}$- and $\mathbf{x}$-coordinate systems is known [i.e., $\boldsymbol{\xi} = \boldsymbol{\xi}(\boldsymbol{x})$ and $\boldsymbol{x} = \boldsymbol{x}(\boldsymbol{\xi})$], we use coordinate transformations in the form of symmetric 4x4 metric tensor $g_{\mu v}$:

$$g_{\mu v} = \begin{bmatrix} g_{00} & g_{01} & g_{02} & g_{03} \\ g_{10} & g_{11} & g_{12} & g_{13} \\ g_{20} & g_{21} & g_{22} & g_{23} \\ g_{30} & g_{31} & g_{32} & g_{33} \end{bmatrix}, \tag{2}$$

whose components are calculated as

$$g_{\mu v} = \frac{\partial x^k}{\partial \xi^\mu}\frac{\partial x^k}{\partial \xi^v}, \text{ for } \mu, v, k = 0, 1, 2, 3, \tag{3}$$

where summation is implied on repeated indices. The time axis is treated in the same manner as the spatial axes, and the fields and operators are expanded to a 4D coordinate transformation. Our convention is that indices denoted with Greek letters run over all time and space coordinates 0,1,2,3 where $t = 0$, while those with Roman letters represent the three spatial components. The tensorial AWE in generalized coordinate system requires a contravariant representation of the metric tensor $g^{\mu v}$ (Shragge and Tapley, 2017). This may be calculated as a point-wise matrix inverse of the covariant metric tensor:

$$g^{\mu v}(t, \boldsymbol{\xi}) = \begin{bmatrix} -1 & \dots & -v_{\xi^j} \\ \vdots & \ddots & \vdots \\ -v_{\xi^i} & \dots & (g^{ij} - v_{\xi^i} v_{\xi^j}) \end{bmatrix}, \tag{4}$$

where the actual matrix values represented by the horizontal, vertical and diagonal ellipsis will depend upon the particular mapping relationship. Similar versions of the metric tensor for 4D coordinate transformation

are reported in literature for Cartesian flow problems (White, 1973; Unruh, 1981; Bergman, 2018).

The metric tensor provides a connection between the $\boldsymbol{\xi}$- and $\mathbf{x}$-coordinate systems, and its time-dependent elements in equation 4 have a clear physical meaning as the mesh velocity vector v. Solving equation 1 requires evaluating the tensorial Laplace-Beltrami operator in generalized ξ-coordinate system (Guggenheimer, 1977):

$$\nabla^2_\xi = \frac{1}{\sqrt{|\mathbf{g}|}} \frac{\partial}{\partial \xi_i} \left(\sqrt{|\mathbf{g}|} g^{ij} \frac{\partial}{\partial \xi_j} \right), \quad \text{i,j} = 1, 2, 3, \tag{5}$$

where $\sqrt{|\mathbf{g}|}$ is the determinant of the covariant metric tensor.

The standard staggered grid (SSG) has been a popular choice for seismic modeling in Cartesian coordinates with a flat free surface assumption due to its simplicity and stability considerations. However, the solution of the AWE in generalized coordinates containing mixed derivatives requires applying computationally expensive high-order interpolations in an SSG scheme to approximate the necessary wavefield values at all required grid locations.

A 2D fully staggered (FSG) scheme (Lebedev, 1964; Lisitsa and Vishnevsky, 2010) provides an alternative approach, where two coupled and complementary grids provide all the required cross-derivatives at every wavefield evaluation point on the mesh (a 3D MFD implementation would require four subgrids). Figure 2 demonstrates the nodal distribution in an FSG, where all components of a scalar u and a vector field $\boldsymbol{v}$ share the same grid points. For the AWE solution, u and $\boldsymbol{v}$ may represent the scalar pressure and particle velocity, respectively. Consequently, all differential operators can be calculated without interpolation, though at the cost of an additional grid (see below). Herein, we utilize an FSG scheme with the mimetic approach (Shragge and Tapley, 2017) to achieve an accurate solution on the irregular and time-varying free-surface boundary.

2.1 Mimetic Finite Differences

Modeling with the time-varying rough free surface requires an accurate implementation of the free-surface boundary condition to maintain the stability of the wave propagation simulation. High-order operators are appealing due to their less dispersive nature compared to low-order counterparts. However, the finite-difference method often fails to provide accurate solutions when the free-surface is not flat since high-order operators lose their numerical accuracy near the boundaries and produce artifacts that severely contaminate and may destabilize the seismic wavefield.

Mimetic methods have been developed as a remedy for such situations, where first-order differential operators (gradient, divergence) are constructed as discrete analogs of their continuum counterparts and mimic the fundamental properties of the physical system, including conservation laws, symmetry, and null-space (Castillo and Miranda, 2013; Shragge and Tapley, 2017). To obtain accurate solutions near the mesh boundaries, we implement MFD operators (de la Puente et al., 2014) that provide a consistent numerical accuracy throughout the computational domain.

We develop a fourth-order MFDTD scheme for the solution of AWE by decomposing the 4D tensorial expression for the Laplacian operator into weighted 4D tensorial gradient:

$$\nabla^{4D}_\xi f = g^{\mu v} \frac{\partial f}{\partial \xi_v}, \quad \mu, v = 0, 1, 2, 3 \tag{6}$$

and 4D tensorial divergence

$$\nabla^{4D}_\xi . \mathbf{v} = \frac{1}{\sqrt{|\mathbf{g}|}} \frac{\partial}{\partial \xi_\mu} \left(\sqrt{|\mathbf{g}|} v^\mu \right), \quad \mu = 0, 1, 2, 3 \tag{7}$$

operators (Shragge and Tapley, 2017). Having defined the metric tensor, equation 1 may be written after algebraic manipulations as

$$\frac{1}{\sqrt{|\mathbf{g}|}} \begin{bmatrix} \frac{\partial}{\partial t} & \nabla^T_\xi \end{bmatrix} \frac{\sqrt{|\mathbf{g}|}}{c^2_\xi} \begin{bmatrix} -1 & -v_{\xi^j} \\ -v_{\xi^i} & (c^2_\xi g^{ij} - v_{\xi^i} v_{\xi^j}) \end{bmatrix} \begin{bmatrix} \frac{\partial P}{\partial t} \\ \nabla_\xi P \end{bmatrix} = F_\xi, \tag{8}$$

where

$$\nabla_\xi = \left[\frac{\partial}{\partial \xi_1}, \frac{\partial}{\partial \xi_2}, \frac{\partial}{\partial \xi_3} \right]. \tag{9}$$

Herein, we evaluate the mimetic gradient $\mathbf{G_i}$ and divergence $\mathbf{D_i}$ within the boundary region and at the free surface. The MFD operators turn into the standard Taylor stencils for the interior region of the mesh. Figure 3 shows an example MFD staggered grid for a grid size $n_1 = 8$, where we assume the seismic wavefield is defined on half-integer points u for one dimension ξ_1. The mimetic gradient operator, when applied to a scalar field, approximates $\mathbf{G_i u} = \mathbf{v_i}$ on $\mathbf{v}$ (green points). As the second step, we apply mimetic divergence $\mathbf{D_i v_i}$ to approximate $\nabla^2 P$, which completes the approximation of the wavefield values on $\mathbf{u}$ (red points). To accurately calculate the wavefield values at the boundaries, wavefields u and $\mathbf{v}$ are not staggered at the boundary and share common grid points. This scheme results in having extra field boundary values that are not usually present in the standard FD discretizations. We calculate the field values at these points $(\mathbf{u_0}, \mathbf{u_8})$ using mimetic operators $\mathbf{G_i}$ and $\mathbf{D_i}$ constructed with the Castillo-Grone method (Castillo and Miranda, 2013). Appendix A provides 1D $\mathbf{G_i}$ and $\mathbf{D_i}$ operators in matrix form.

3 NUMERICAL EXAMPLES

We define our time-varying sea surface using the Pierson and Moskowitz (1964) model, which specifies the whole wave spectrum of a fully developed sea based on a persistent wind speed. A modified version of the spectrum

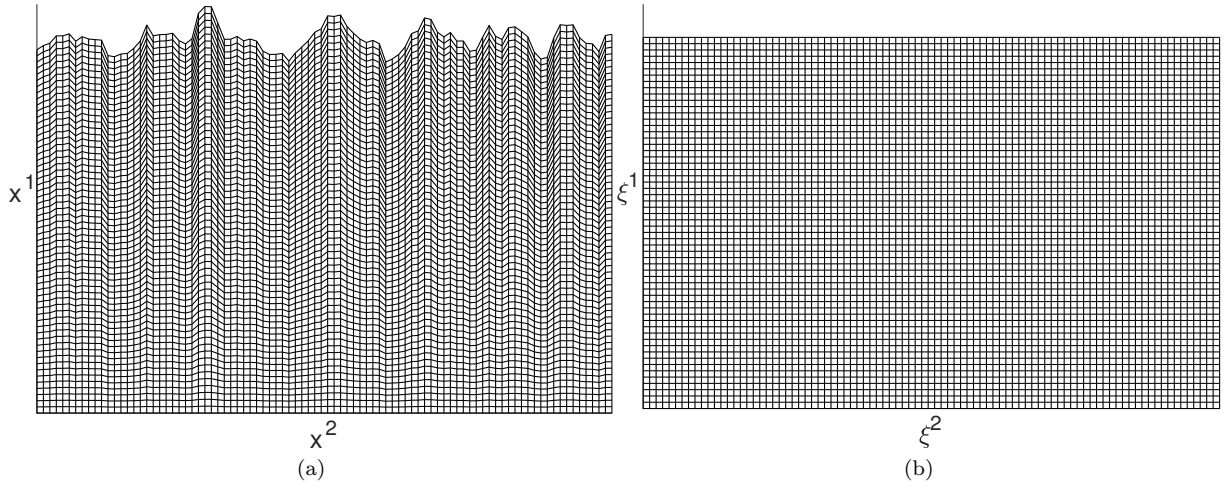

Figure 1. Mapping between (a) the physical and (b) the computational domains.

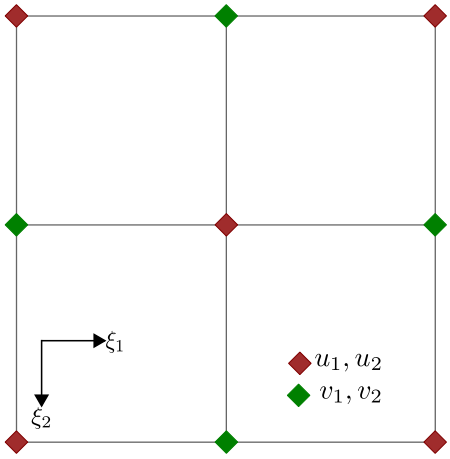

Figure 2. Node distribution in a 2D FSG scheme. The distance between red and green diamonds is half a grid spacing. Note that all the components of u and v are defined at the same grid point.

including a directivity term (Laws and Kragh, 2002) is written in the wavenumber domain as

$$S(k_x, k_y) = \frac{N\alpha}{2k^4} \exp\left(\frac{-\beta^2 g^2}{k^2 U^4}\right) \cos^{2s}\left(\frac{\theta}{2}\right), \qquad (10)$$

where $\alpha = 0.0081$ and $\beta = 0.74$ are constants, $k = |\boldsymbol{k}| = |(k_x, k_y)|$ is the wavenumber, g is the gravitational acceleration, U is the wind speed measured 19 m above the sea surface, θ is the azimuth angle relative to wind direction, N is a normalization factor, and s is an empirical frequency-dependent spreading factor. Here, we assume that the sea-surface height has Gaussian statistics and introduce time-varying effects by adding random perturbations to the power spectrum. Using the modeled sea surface, we specify a 4D generalized coordinate system using linear Bézier interpolation functions (Shragge, 2014) in the (vertical) x^3 coordinate dimension:

$$\begin{bmatrix} x^0 \\ x^1 \\ x^2 \\ x^3 \end{bmatrix} = \begin{bmatrix} \xi^0 \\ \xi^1 \\ \xi^2 \\ \xi^3 + T(1 - \frac{\xi^3}{a}) \end{bmatrix}, \qquad (11)$$

where $x^0 = \xi^0 = t$ is the time dimension, $x^1 = \xi^1$ and $x^2 = \xi^2$ are lateral dimensions, $T = T(t, \xi^1, \xi^2)$ is the time-dependent sea-surface model, and a is the maximum depth. Figure 1 represents an irregular model in physical Cartesian $\mathbf{x}$-coordinates where the surface grid layer coincides with sea-surface topology. We use the coordinate transformation relationship in equation 11 to map a C^2-smooth curvilinear grid in physical domain $\mathbf{x}$ to a uniform rectangular grid in computational ξ domain on which we solve the AWE. We simulate the time-varying behavior of the sea surface by moving the

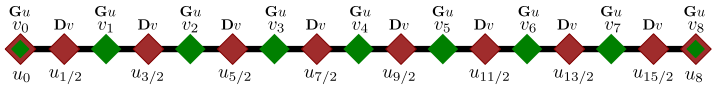

Figure 3. Example of a 1D MFD staggered grid for $n_1 = 8$ points. We assume wavefield P is defined on half-integer points u.

grid points in the vertical direction ξ^3, while holding their ξ^1 and ξ^2 coordinate directions constant throughout the wavefield extrapolation (equation 11).

3.1 Modeling with an extreme sea state

For our first numerical example, we conduct a 2D wavefield simulation with an exaggerated maximum sea surface wave height of 20 m and an extreme sea surface wave speed in the horizontal direction. The water velocity is 1500 m/s and the source is a zero phase Ricker wavelet with 30 Hz dominant frequency. Even though seismic data acquisition would not take place in such conditions, our aim here is just to demonstrate the accuracy of MFD wavefield simulation on time-varying grids. Figure 4 presents four evolving wavefield snapshots computed in generalized coordinates and then interpolated back to a Cartesian grid. The spatial variation of the sea surface in the vertical direction accelerates and decelerates all the components of particle velocity of the acoustic wavefield. Despite the extreme movement of the water layer, the simulation is stable and free of artificial numerical fluxes usually introduced by an inaccurate free-surface boundary condition implementation (Shragge and Tapley, 2017). Interaction of the acoustic wavefield with the moving surface distorts the acoustic wavefield and causes a complex down-going wavefront with spatially varying amplitude (de)focusing effects.

3.2 Rough sea effects on ghosts and multiples

To demonstrate more realistic rough sea effects on seismic data, we conduct a wavefield simulation test with a more realistic sea state of 4 m of significant wave height (i.e., $\pm$2m with respect to a flat surface). Because we are interested in acoustic waves reflecting off of the irregular rough sea surface, we restrict our modeling domain to just the water layer. This allows us to better demonstrate the effects of time-varying seas on an increasing order of the ghost reflections and multiples. To achieve a clear separation between all events, we place the source at 140 m, far deeper than in typical seismic acquisition. Here, the water layer is 150 m deep with a velocity of $c = 1500$ m/s and the source is a Ricker wavelet with 45 Hz dominant frequency.

Figures 5a-c show three shot gathers obtained with flat, frozen (i.e., where the sea-surface is non-flat and static), and a time-varying rough sea surface, respectively. Compared to the flat sea response, all events reflected from the non-flat sea surface have deviations in their travel time to various extents, as is evident from the non-hyperbolic ghost and multiple reflections in Figures 5b-c. When the sea surface is moving, these effects are inherently time-dependent and manifest as non-systematic alterations in the acoustic wavefield (Figure 5c).

3.3 Modeling with a more realistic acquisition

To further investigate the rough sea effects on the source and receiver ghost, we computed a typical receiver response at a point located at 6 m below the sea surface. The sea surface has 4 m of significant wave height and was calculated with 19 m/s wind speed. Figure 7 shows a comparison of the seismic trace measured again under a flat, frozen and a time-varying sea surface. The source is a zero phase Ricker wavelet with 60 Hz central frequency and has a buoyed deployment where the source depth is suspended at its nominal depth relative to the sea-surface immediately above the air gun (Laws and Kragh, 2002). The initial pulse shape and amplitude are almost identical for the flat and frozen sea with a small difference in the source ghost reflection. Receiver ghosting, on the other hand, seems to be more sensitive to the variations at the sea surface, as may be seen from the considerable amplitude and travel-time perturbations. In the case of a moving surface, the distortions in source ghost response also become visible.

4 DISCUSSION

The MFDTD implementation on an FSG increases the accuracy of the tensorial AWE solution for complex geometry. Accurate implementation of the free-surface boundary condition provides stability in the presence of a time-varying rough free surface, where our tests of purely Taylor-based coefficients were demonstrably unstable. Also, the presence of cross-derivative terms makes FSGs a natural choice for implementing wavefield propagation in more complex media (e.g., anisotropic). The results show that the rough sea surface effects on ghost and multiples increase as the order of the events increases. Even though some demultiple algorithms can handle these distortions to some extent through least-squares adaptive filtering, deterministic deghosting algorithms are usually very sensitive to the changes in the time delay between primary and ghost reflections. Hence, a flat sea surface assumption will likely cause deghosting algorithms to fail to produce

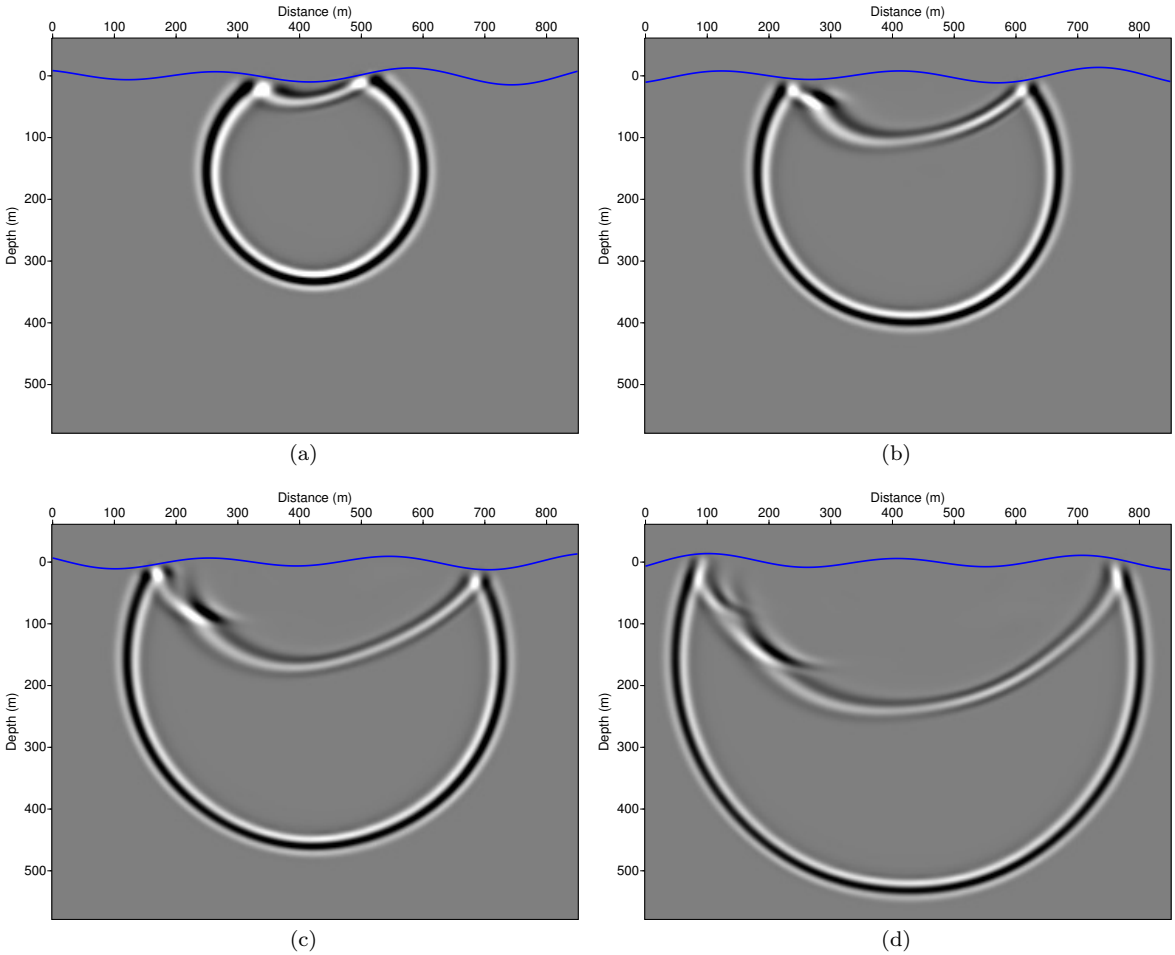

Figure 4. The wavefield snapshots for $t = 0.17,\ 0.26\,0.35$ and 0.44 s. The time-varying sea surface is illustrated by the different blue lines in the four panels. In this extreme example, note that the sea surface introduces wavefield scattering that would not exist in a flat surface.

satisfactory results when using only single-component hydrophone data. In addition to the travel-time perturbations, time-dependent variations in sea height cause wavefield (de)focusing, directivity changes, and changes the sea surface reflectivity, which are important parameters contributing to the quality and accuracy of deghosting results.

The effect of the rough sea on the source ghost is small when compared to the receiver ghost. Our examples demonstrate that the rough sea perturbs both the amplitudes and the travel times of the ghost reflections. We obtain an almost identical source ghost response with the flat and the frozen sea surface, whereas there is a small perturbation to the travel time of the receiver ghost. Conversely, a moving sea surface visibly alters the source ghost, and has a more significant impact on the amplitudes and especially on travel times of the receiver ghost.

Our results imply that a careful consideration of time-varying rough sea effects is necessary during data processing to achieve reliable and high-resolution results. We expect the inaccuracies in deghosting and demultiple applications to complicate the seismic signal (i.e., primaries) and greatly increase interpretation uncertainty. In addition, the time-varying nature of the errors severely reduces the repeatability of time-lapse (4D) seismic data. Laws and Kragh (2002) demonstrates that rough sea effects manifest as false events in time-lapse difference data even for relatively calm sea conditions.

Imaging with multiples usually requires using a least-squares migration procedure to reduce the cross-talk noise introduced by correlating unrelated multiples (Zhang and Schuster, 2014). These algorithms treat multiples as signal, and iteratively update the seismic image using the difference between real and synthetic multiple models. Hence, they are very sensitive to the accuracy of the demultiple process and to accurate modeling of multiples with wavefield extrapolation. Our examples demonstrate that incorporating dynamic sea surface variations is essential for generating multiples

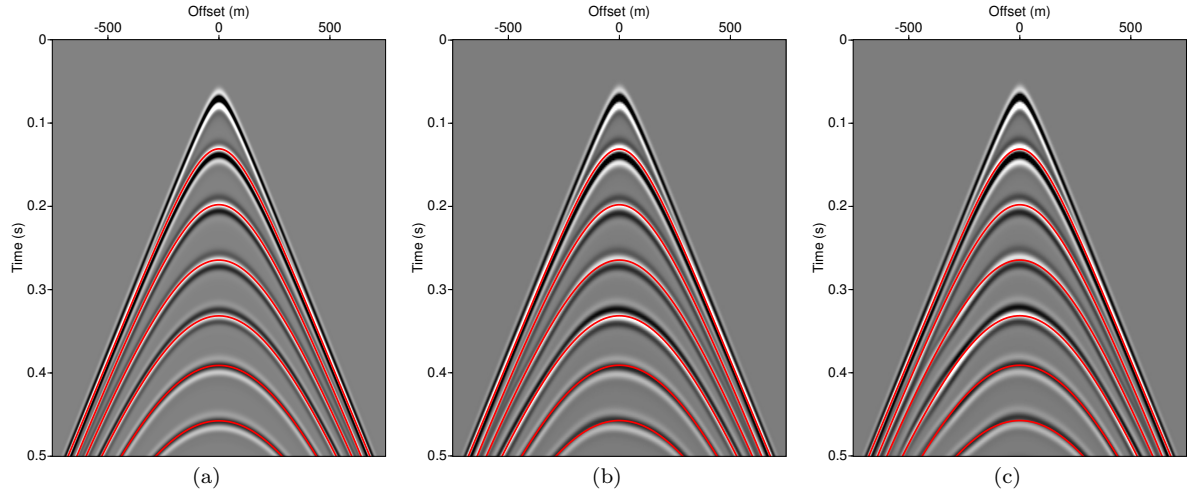

Figure 5. Shot gathers modeled with (a) flat, (b) frozen, and (c) time-varying sea surface profiles. The theoretical travel times are illustrated by the red curves. Note that rough sea conditions introduce traveltime perturbations to ghost and multiple reflections.

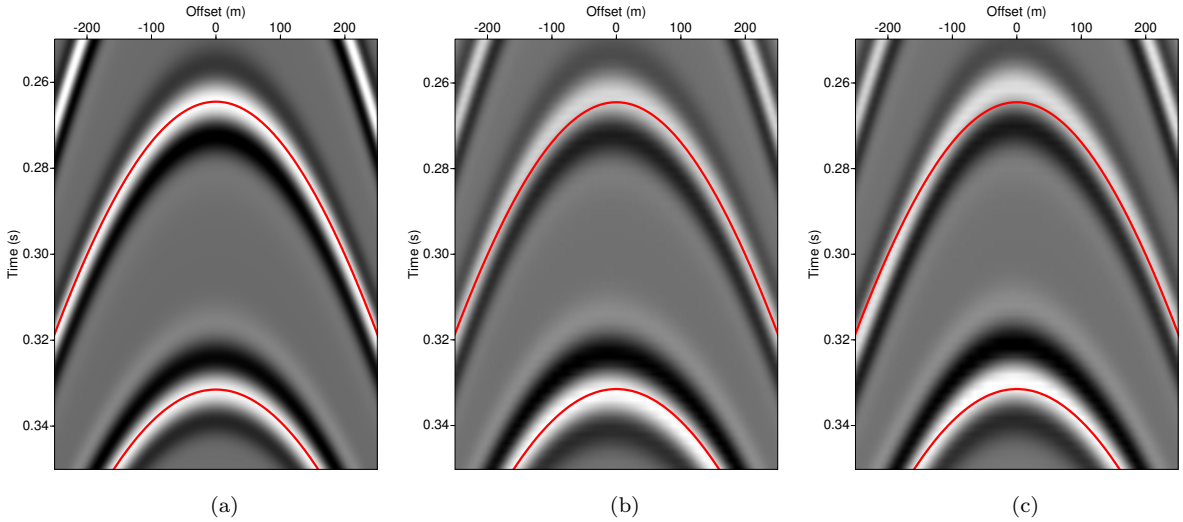

Figure 6. Zoom panels for the shot gathers in Figure 5. Here, panels show data modeled with (a) flat, (b) frozen, and (c) time-varying sea surface profiles.

with correct travel times, and hence obtaining reliable results.

Finally, despite all the benefits, our implementation comes with additional computational overhead. The memory and computational cost of a 2D FSG approach are roughly two times that of an SSG implementation due to additional staggered grids. In addition, semi-analytic geometric transformations require calculation of 4×4 acoustic metric tensor coefficients in equation 4 for all grid points at every time step. Even though spatial components of the acoustic metric (g^{ij}) are constant throughout the simulation, mesh velocities (v_{ξ^j}) are time-dependent and need to be updated at every time step. Moreover, sea surface profile calculation adds a minor overhead to the overall computational complexity.

5 CONCLUSIONS

We present an MFD approach for solving the tensorial acoustic wave equation on time-varying grids. The method is based on an FSG comprised of two complementary staggered grids that provide all required cross-derivatives for the MFD-AWE solution on a generalized grid. The accurate simulation of wave propagation with a time-varying sea surface requires a special treatment near the free-surface boundary. Finite-difference solu-

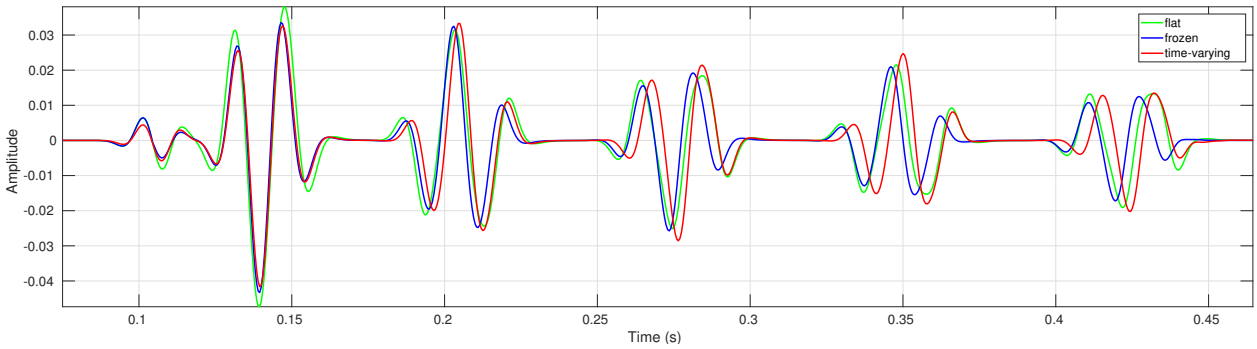

Figure 7. Seismic data measured by a receiver located at 6 m. below the sea surface at a 125 m source-receiver offset. Note that the rough sea affects both the amplitude and the arrival time of the ghost reflection.

tions of AWE are known to be unstable in the presence of a non-flat free surface due to difficulties in accurately implementing the free-surface boundary conditions. We show that the MFD approach allows for accurate implementation of the free-surface boundary condition in the presence of rough sea conditions and provides a uniformly accurate solution over the entire mesh. Although our implementation is 2D, we provide formulation for 3D implementation throughout the text.

6 ACKNOWLEGDMENTS

The authors acknowledge the support of sponsors of the Center for Wave Phenomena consortium at the Colorado School of Mines. Reproducible numerical examples were generated using the Madagascar package (http://www.ahay.org). Analytic coordinate system geometry results were verified using the Mathematica software package (http://www.wolfram.com/mathematica/).

REFERENCES

Bergman, D. R., 2018, Computational acoustics: Theory and implementation: Wiley.

Castillo, J. E., and G. F. Miranda, 2013, Mimetic discretization methods: CRC Press.

de la Puente, J., M. Ferrer, M. Hanzich, J. Castillo, and J. M. Cela, 2014, Mimetic seismic wave modeling including topography on deformed staggered grids: Geophysics, **79**, no. 3, T125–T141.

Egorov A., S. Glubokovskikh, A. Bóna, R. Pevzner, B. Gurevich, and M. Tokarev, 2018, How rough sea affects marine seismic data and deghosting procedures: Geophysical Prospecting, **66**, 3–12.

Guggenheimer, H., 1977, Differential geometry: Dover Publications Inc.

Komatitsch, D., and J. P. Vilotte, 1998, The spectral-element method: an efficient tool to simulate the seismic response of 2D and 3D geological structures: Bulletin of the Seismological Society of America, **88**, 368–392.

Laws, R., and E. Kragh, 2002, Rough seas and time-lapse seismic: Geophysical Prospecting, **54**, 475–485.

Lebedev, V., 1964, Difference analogues of orthogonal decompositions, basic differential operators and some boundary value problems: USSR Computational Mathematics and Mathematical Physics, **5**, 449–465.

Lisitsa, V., and D. Vishnevsky, 2010, Lebedev scheme for the numerical simulation of wave propagation in 3D anisotropic elasticity: Geophysical Prospecting, **58**, 619–635.

Ogilvy, J. A., 1987, Wave scattering from rough surfaces: Reports on Progress in Physics, **50**, 1553–1608.

Pierson, W. J., and L. Moskowitz, 1964, A proposed spectral form for fully developed wind seas based on the similarity theory of S. A. Kitaigorodskii: Journal of Geophysical Research, **69**, 5181–5190.

Shragge, J., 2014, Solving the 3D acoustic wave equation on generalized structured meshes: A finite-difference time domain approach: Geophysics, **79**, no. 6, T363–T378.

Shragge, J., and B. Tapley, 2017, Solving the tensorial 3D acoustic wave equation: A mimetic finite-difference time-domain approach: Geophysics, **82**, no. 4, T183–T196.

Thorsos, E. I., 1988, The validity of the kirchhoff approximation for rough surface scattering using a gaussian roughness spectrum: The Journal of the Acoustical Society of America, **83**, 78–92.

Unruh, W. G., 1981, Experimental black hole evaporation: Physical Review Letters, **46**, 1351–1353.

White, R. W., 1973, Acoustic ray tracing in moving inhomogeneous fluids: The Journal of the Acoustical Society of America, **53**, 1700–1704.

Zhang, D., and G. T. Schuster, 2014, Least-squares reverse time migration of multiples: Geophysics, **79**, no. 1, P11–P21.

7 APPENDIX A

MFD OPERATORS

The 1D MFD gradient operator used in the numerical examples is given by

$$\mathbf{G_i} = \frac{\mathbf{1}}{\mathbf{\Delta\xi_i}} \begin{bmatrix} \frac{-1152}{407} & \frac{10,063}{3256} & \frac{2483}{9768} & \frac{-3309}{3256} & \frac{2099}{3256} & \frac{-697}{4884} & 0 & \dots & \dots & \dots \\ 0 & \frac{-11}{12} & \frac{17}{24} & \frac{3}{8} & \frac{-3}{24} & \frac{1}{24} & 0 & \dots & \dots & \dots \\ 0 & \frac{1}{24} & \frac{-9}{8} & \frac{9}{8} & \frac{-1}{24} & 0 & 0 & \dots & \dots & \dots \\ 0 & 0 & \frac{1}{24} & \frac{-9}{8} & \frac{9}{8} & \frac{-1}{24} & 0 & \dots & \dots & \dots \\ \vdots & \vdots & \vdots & \ddots & \ddots & \ddots & \ddots & \vdots & \vdots & \vdots \\ \dots & \dots & \dots & \dots & \frac{1}{24} & \frac{-9}{8} & \frac{9}{8} & \frac{-1}{24} & 0 & 0 \\ \dots & \dots & \dots & \dots & 0 & \frac{1}{24} & \frac{-9}{8} & \frac{9}{8} & \frac{-1}{24} & 0 \\ \dots & \dots & \dots & \dots & \frac{-1}{24} & \frac{5}{24} & \frac{-3}{8} & \frac{-17}{24} & \frac{11}{12} & 0 \\ \dots & \dots & \dots & \dots & \frac{697}{4884} & \frac{-2099}{3256} & \frac{3309}{3256} & \frac{-2483}{9768} & \frac{-10,063}{3256} & \frac{1152}{407} \end{bmatrix}, \tag{A-1}$$

where dots indicate the repetition of stencil coefficients along the corresponding direction. The 1D MFD divergence operator is given by

$$\mathbf{G_i} = \frac{\mathbf{1}}{\mathbf{\Delta\xi_i}} \begin{bmatrix} 0 & 0 & 0 & 0 & 0 & 0 & 0 & \dots & \dots & \dots \\ \frac{-4751}{5192} & \frac{909}{1298} & \frac{6091}{15,576} & \frac{-1165}{5192} & \frac{129}{2596} & \frac{-25}{15,576} & 0 & \dots & \dots & \dots \\ 0 & \frac{1}{24} & \frac{-9}{8} & \frac{9}{8} & \frac{-1}{24} & 0 & 0 & \dots & \dots & \dots \\ 0 & 0 & \frac{1}{24} & \frac{-9}{8} & \frac{9}{8} & \frac{-1}{24} & 0 & \dots & \dots & \dots \\ \vdots & \vdots & \vdots & \ddots & \ddots & \ddots & \ddots & \vdots & \vdots & \vdots \\ \dots & \dots & \dots & \dots & \frac{1}{24} & \frac{-9}{8} & \frac{9}{8} & \frac{-1}{24} & 0 & 0 \\ \dots & \dots & \dots & \dots & 0 & \frac{1}{24} & \frac{-9}{8} & \frac{9}{8} & \frac{-1}{24} & 0 \\ \dots & \dots & \dots & \dots & \frac{25}{15,576} & \frac{-129}{2596} & \frac{1165}{5192} & \frac{-6091}{15,576} & \frac{-909}{1298} & \frac{4751}{5192} \\ \dots & \dots & \dots & \dots & 0 & 0 & 0 & 0 & 0 & 0 \end{bmatrix}, \tag{A-2}$$

where three dots indicate the repetition of elements along corresponding diagonal.